International Journal of Heat and Fluid Flow 103 (2023) 109194

Contents lists available at ScienceDirect

International Journal of Heat and Fluid Flow

journal homepage: www.elsevier.com/locate/ijhff

Experimental investigation of turbulent boundary layer dynamics via active manipulation of large-scale structures

Mitchell Lozier *, Flint O. Thomas, Stanislav Gordeyev

Institute for Flow Physics and Control, Dept. of Aerospace and Mech. Engineering, University of Notre Dame, Notre Dame, IN 46556, USA

ARTICLE INFO

Keywords:
Turbulent boundary layer
Large-scale structures
PIV

ABSTRACT

The dynamic response of a zero pressure gradient turbulent boundary layer (TBL) to an active flow control actuator was experimentally studied using continous laser particle imaging velocimetry (PIV). In previous experiments using a single hot-wire, it was shown that the synthetic large-scale structure (LSS) introduced by the plasma-based actuator, located in the outer region of TBL, had a strong modulating and reorganizing effect on the near-wall turbulence. In the study reported here, an actuator, optimized for the experimental TBL, was placed at the upper boundary of the log-linear region of the TBL to produce a spanwise uniform, periodic synthetic LSS in order to study the response of the TBL to these large-scale perturbations. Planar PIV over a narrow streamwise region was used to measure the time-resolved, two-dimensional velocity downstream of the actuator at a series of streamwise point locations. Using PIV, the modulating effect of the synthetic LSS on the near-wall turbulence is described in more detail. The results are discussed and compared with previous hot-wire measurements and numerical simulations of the actuated TBL.

1. Introduction

It is now widely recognized that vortical large-scale structures (LSS) play a key role in governing the dynamics of wall bounded turbulent flows. The effect of these LSS in turbulent boundary layers (TBL) on technologically relevant flow properties (e.g., friction drag, noise generation, aero-optical distortions, flow separation etc.) have been extensively documented (Robinson, 1991; Guala et al., 2006; Hutchins and Marusic, 2007). The influence of the LSS on the TBL dynamics was shown to increase with Reynolds number (Hutchins and Marusic, 2007). The dynamics of the LSS have also been shown to be correlated with the near-wall small-scale turbulence (Hutchins and Marusic, 2007; Mathis et al., 2011). It was demonstrated that the large-scale structures alter turbulence characteristics by imposing mean velocity changes on the near-wall region, referred to as superposition, and they also directly modulate the amplitude and organization of the near-wall turbulent motions (Hutchins and Marusic, 2007; Andreolli et al., 2023). These findings suggest the potential effectiveness of flow control strategies focused on altering the LSS dynamics to achieve desired technological goals (e.g., reduced drag, noise reduction and separation control). Such strategies could lead to significant performance gains and cost savings. However, to date, this potential remains largely unrealized due, in large part, to an incomplete understanding regarding the production, subsequent development and then interaction of these LSS within both the inner and outer regions of the TBL.

In general, the prevailing views of TBL dynamics fall into two broad groups: (1) those that focus on the influence of outer layer LSS on the near wall turbulence generation mechanism; the so-called" top-down" mechanism, and (2) those that view the near wall mechanism as largely autonomous, and the outer LSS as a consequence of the near-wall turbulence; the “bottom-up” mechanism. Several different models have sought to couple the two regions, with one of the oldest and most notable being the Attached Eddy Model (de Silva et al., 2016), which suggests self-similar eddies as a typical topology of the structure. Mathis et al (Mathis et al., 2011) also modelled these interactions using a correlation-based statistical model where the near-wall effects are predicted from the statistics of the large-scale structures. Both models have proven incredibly useful in understanding the structure of turbulent flows but are limited in that they are statistical in nature and fail to capture the underlying dynamic interaction of the structures. Resolvent analysis is a recent method that overcomes this limitation by looking at spatial–temporal interactions in wall-bounded turbulent flows, thereby providing insight into the dynamics of the structures (McKeon and Sharma, 2010). Resolvent analysis has proven successful in identifying a

* Corresponding author.
E-mail addresses: mlozier@nd.edu (M. Lozier), fthomas@nd.edu (F.O. Thomas), sgordeye@nd.edu (S. Gordeyev).

https://doi.org/10.1016/j.ijheatfluidflow.2023.109194
Received 30 January 2023; Received in revised form 15 June 2023; Accepted 1 July 2023
Available online 19 July 2023
0142-727X/© 2023 Elsevier Inc. All rights reserved.

key wavenumber-frequency "kernel" or "skeleton" of turbulent pipe flow and answering fundamental questions about the structure of wall-bounded turbulent flows, see e.g., (Sharma and McKeon, 2013).

A majority of studies and models regarding the relationship between the near-wall and outer layer large-scale structures deal with natural, un-manipulated TBLs and apply various conditional averaging techniques to study their interactions (Mathis et al., 2011). We take the view that to clarify the dynamics of the large-scale structure, one needs to analyse the flow's response to an external large-scale perturbation. Such a dynamic systems approach in which the boundary layer is perturbed using an actuator is particularly well suited to gaining insights regarding the underlying flow physics which is essential for the design of novel active flow control strategies.

More specifically, this approach would artificially introduce a well-defined perturbation with a given frequency and/or spatial scale that allows quantification of the nonlinear TBL response. This approach then allows, for instance, the study of triadic interactions between various scales of motion. It also provides a well-defined phase reference by which to perform a phase-locked analysis. In this manner, periodic perturbations have been experimentally introduced into a turbulent boundary layer through a dynamic (temporally oscillating) wall roughness, which provides a reference phase to isolate synthetic large-scale structures and small-scale flow structures (Jacobi and McKeon, 2011; Jacobi and McKeon, 2013; McKeon et al., 2018). Results of these dynamic roughness experiments showed that the synthetic large-scale motions had a strong effect on triadically coupled small-scale motions, and a phase-locking or reorganizing effect was observed in the near-wall structures of the TBL as a result (McKeon et al., 2018). In contrast, instead of introducing the perturbation very close to the wall, Ranade et al. (Ranade et al., 2019) performed an experimental study where the perturbation was introduced in the outer region, as a forced shear layer, and the turbulence inside the boundary layer was found to be both amplified and modulated by the external forcing. In summary, the introduction of prescribed periodic perturbations has proven to be an effective way to characterize turbulent boundary layer dynamics.

2. Approach and experimental set-up

In previous work (Lozier et al., 2021; Lozier et al., 2020), large-scale spanwise vorticity was introduced into the outer region of the TBL using a novel flow control device, which was termed the Active Large-Scale Structure Actuator (ALSSA), see Fig. 1(a). The ALSSA device was configured to produce a spanwise uniform, plasma-induced, pulsed jet along the top surface of the actuator that introduces coherent spanwise vorticity into the TBL at a specified frequency and user-selected wall-normal location. To isolate the interactions of interest, the experimental studies were performed at $Re_\theta = 1770$, which is low enough that there were no significant naturally occurring organized energetic large-scale structures in the outer region of the turbulent boundary layer, as demonstrated in Fig. 3(a) (Hutchins and Marusic, 2007; Lozier et al., 2021). This approach allows for the controlled introduction of a synthetic and periodic large-scale structure into the TBL, thereby emulating a higher Reynolds number flow. The fixed forcing frequency provides a well-defined reference by which to phase-lock the measurement of the TBL response and provides a clear separation between the large-scale structure and the resulting changes to the TBL dynamics. The key advantage of using the plasma-based ALSSA method of actuation is that it introduces the periodic structure at a user-selected location away from the wall without directly interfering with the canonical near-wall turbulent structures at the point of actuation.

The experiments presented here were performed in a low-turbulence, subsonic, in-draft wind tunnel located at the University of Notre Dame. To create a canonical turbulent boundary layer, a 2-meter-long by 0.6-meter-wide boundary layer development plate was installed along the centre height of the tunnel test section. The key canonical turbulent boundary layer parameters, measured at $x = 3\delta$ downstream of the actuator location, are summarized in Table 1. The experimental canonical TBL was measured to have a log-linear region from $y^+ \approx 50 -$

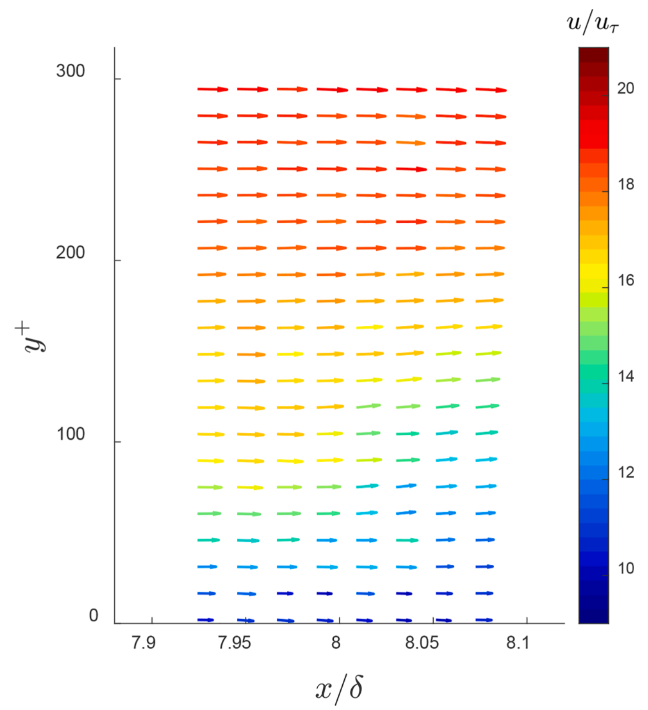

Fig. 2. Instantaneuos velocity vector field for canoncial turbulent boundary layer at $x = 8\delta$.

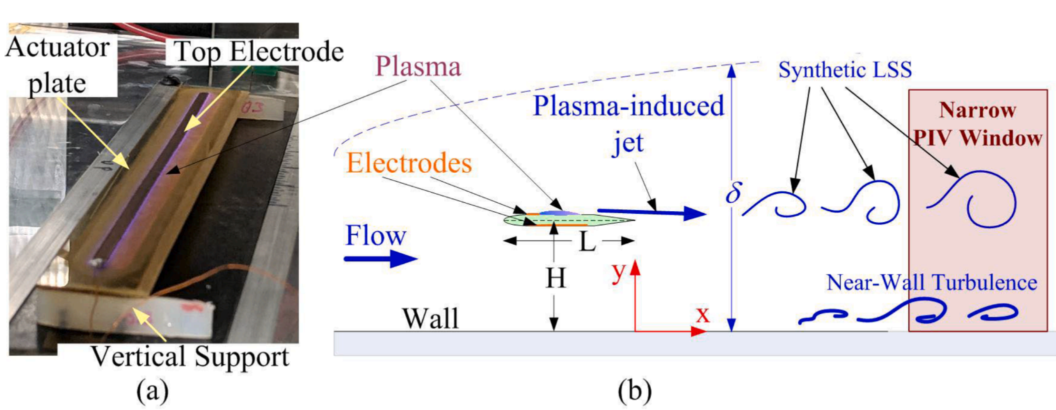

Fig. 1. (a) Picture of plasma-based ALSSA device and (b) schematic of experimental PIV set-up.

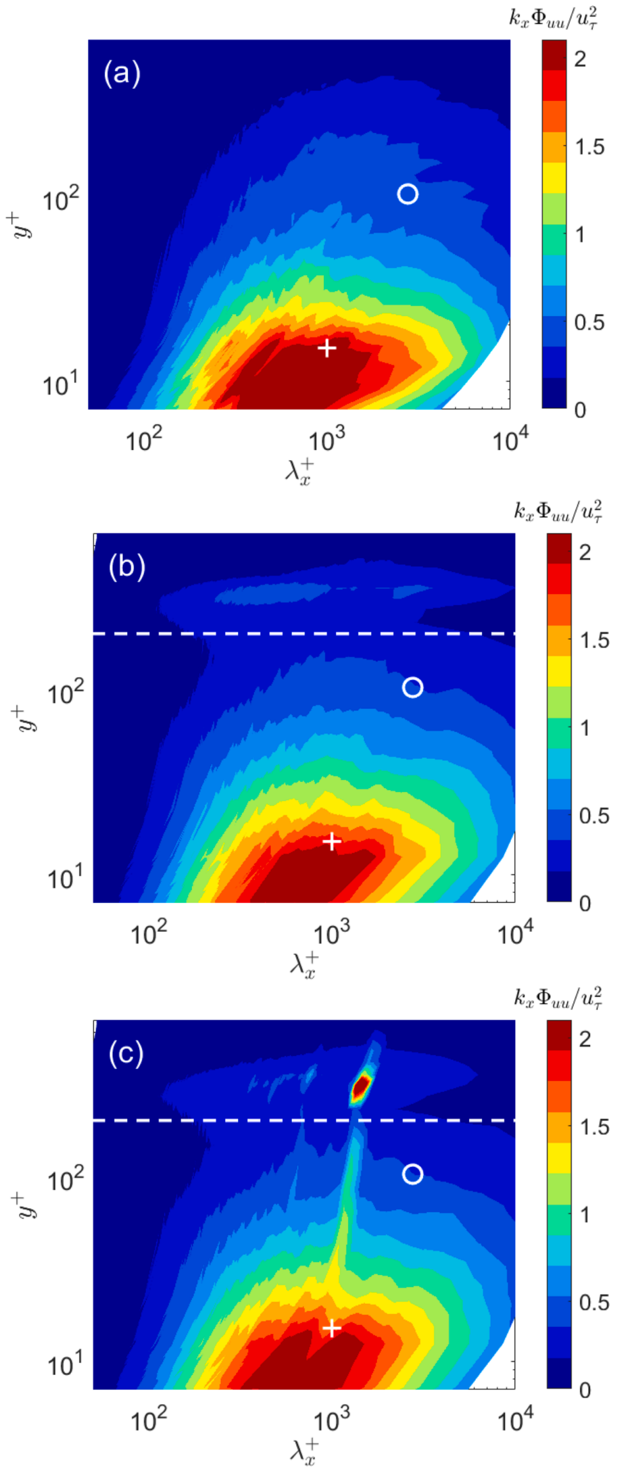

Fig. 3. Premultiplied streamwise velocity energy spectra for (a) canonical (b) plate-only and (c) plasma on cases. Cross marks inner peak ($y^+ = 15$, $\lambda_x^+ = 1000$). Open circle marks theoretical location of outer peak ($y^+ = 3.9Re_\tau^{1/2}$, $\lambda_x^+ \approx 2700$). Dashed line represents actuator plate location $x = 3\delta, H^+ = 200$, $f_p = 80Hz$.

Table 1
Turbulent boundary layer parameters.

δ	U_∞	u_τ	C_f	Re_θ	Re_τ
33.4 mm	6.95 m/s	0.304 m/s	0.0039	1,770	690

200 as seen in Fig. 4(a). The friction velocity (u_τ) was deduced using the Clauser chart method with an approximate relative error of $\varepsilon_{u_\tau} = \pm 0.09\%$. The resulting estimation of the friction velocity for the experimental canonical boundary layer was $u_\tau = 0.304 \pm 0.027 m/s$.

The ALSSA device used in these experiments was built from a 2 mm thick (0.06δ) rectangular sheet of Ultem dielectric polymer. To create the spanwise uniform plasma jet, electrodes made from thin copper foil were installed on both sides of the actuator plate. The alternating current dielectric barrier discharge (AC-DBD) plasma jet produced on the top side of the actuator plate was generated using a high voltage AC source. This source provided a 40 kV peak-to-peak sinusoidal waveform excitation to the electrodes at a frequency of 4 kHz which resulted in a quasi-steady plasma jet. The streamwise length of the actuator was chosen to be $L = 32mm (< 1\delta)$ to both minimize the wake downstream of the actuator plate and prevent any arcing between the plasma electrodes. The spanwise length of the actuator plate was $W = 25cm (8\delta)$ wide to ensure a primarily spanwise-uniform actuation. Symmetric airfoil-shaped vertical supports were used to position the actuator plate at a fixed wall-normal distance of $H/\delta = 0.3 (H^+ = 200)$. To introduce periodic forcing, the sinusoidal waveform creating the plasma jet was modulated by a square wave at the forcing frequency, $f_p = 80Hz (f_p\delta/$

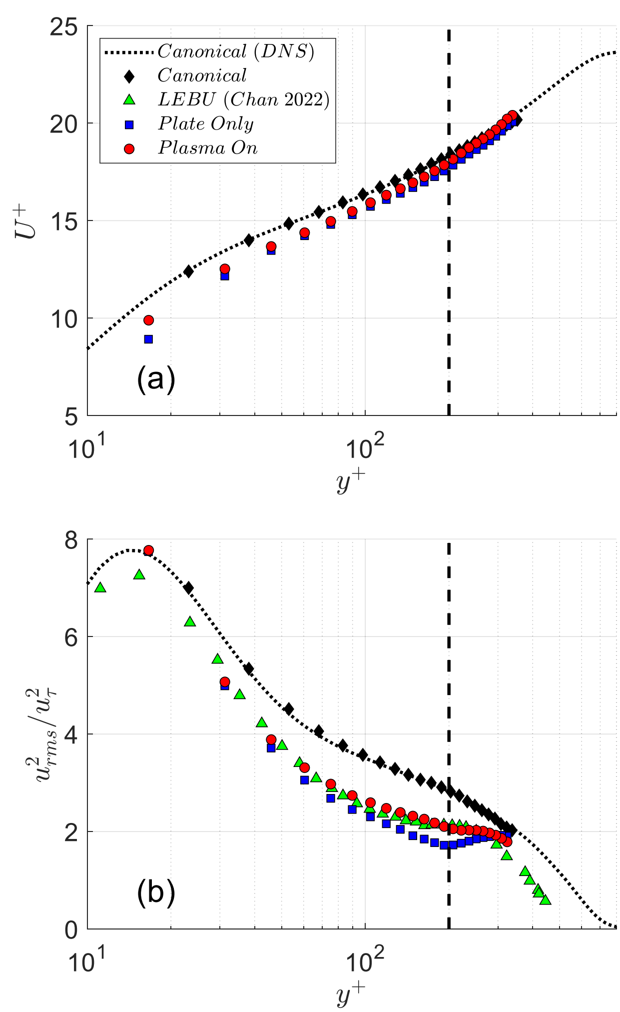

Fig. 4. (a) streamwise mean velocity and (b) streamwise turbulence intensity. PIV turbulence intensities corrected for spatial averaging (Lee et al., 2016). Vertical dashed line indicates actuator location. Dotted line is canonical DNS data (Jiminez, 2010). Green triangles represent LES data for LEBU (Chan et al., 2022) $x = 8\delta, H^+ = 200, f_p = 80Hz$. (For interpretation of the references to colour in this figure legend, the reader is referred to the web version of this article.)

$U_\infty = 0.4$) with a fifty percent duty cycle. These actuation parameters were chosen for the present experiments because they were shown in previous work (Lozier et al., 2021; Lozier et al., 2020) to produce the greatest modulation effect in the near-wall region. A schematic of the experimental set-up is shown in Fig. 1(b). To quantify the effect of the synthetic large-scale structure on the near-wall turbulence a time-resolved, planar PIV system with a continuous laser source was used. To perform PIV measurements, the flow was seeded with Di-Ethyl-Hexyl-Sebacate (DEHS) particles (diameter < 1 μm) at the tunnel inlet. The measurement region was illuminated with a 2 W continuous 532 nm laser (Laser Quantum Excel), formed into a light sheet ($< 1mm$spanwise thickness) and directed through the top of the test section. Because the source was a continuous laser, the laser sheet was focused onto a small streamwise region ($\Delta x = 6mm$, $\Delta x = 0.2\delta$)to achieve the light intensity required to perform PIV measurements. Fig. 2 presents an instantaneous velocity vector field measured using this PIV technique and shows the limited streamwise extent of these measurements. Additionally, because there was no pulse provided by the laser source to create short exposures of the particles and short interval image pairs, a high-speed camera was used. Images were captured with a Phantom v2512 high-speed camera using a $5\mu s$ exposure at a resolution of 384×280 pixels. This exposure time resulted in a balance between light intensity and the sharpness of particle images with the continuous laser source. The frame rate of the camera was 20 kHz ($\approx 100U_\infty/\delta$) which resulted in particle displacements between successive images ($\approx 4px$) that were suitable for the intended spatial resolution of the measurement. Processing of particle images and the calculation of velocity vectors were done using DaVis 10 software. Interrogation windows of $16 \times 16px^2$ with 25% overlap were used for the vector field calculation. The resulting spatial resolution of the computed velocity vector fields was $\Delta x^+ = \Delta y^+ = 15$ as shown in Fig. 2. The error in the calculated velocity, estimated by the DaVis software, was $\varepsilon_U < 0.005U_\infty$ ($\varepsilon_U < 0.1u_\tau$).

The PIV acquisition and plasma forcing were triggered simultaneously such that the collected data was phase-locked to the plasma actuation cycle. The measurements presented here were taken at streamwise locations of $x = 3, 5, \text{and} 8\delta$ downstream of the trailing edge of the actuator. The actuator was fixed $140cm$ downstream of the leading edge of the boundary layer development plate. This continuous laser, planar PIV configuration resulted in measurements of the two-dimensional velocity field at specific streamwise locations that were time resolved and which were also spatial resolved in the wall-normal direction.

3. Results

The premultiplied streamwise velocity energy spectra for the canonical and actuated turbulent boundary layers, measured immediately downstream of the actuator, are presented in Fig. 3 for reference. These spectra were originally measured in previous work using hot-wire (Lozier et al., 2021).

In each case the inner peak in the premultiplied spectra lines up well with the expected location marked by a white cross (Sharma and McKeon, 2013). In the canonical spectra, Fig. 3(a), there is no large-scale outer peak present in the spectra as expected for a low Reynolds number TBL. The expected location of a natural large-scale structure (Hutchins and Marusic, 2007) is indicated by the white circle demonstrating that there is no significant naturally-occurring large-scale structure present in the canonical experimental TBL. In Fig. 3(b) the addition of the actuator plate causes a moderate reorganization of energy in the outer region consistent with the introduction of the plate's wake. In Fig. 3(c) the addition of plasma forcing creates a clear strong peak in the spectra representing the synthetic periodic large-scale structure introduced by the actuator. The peak is strongest just above the actuator location, marked by the dashed line, and corresponds to a streamwise wavelength of $\lambda_x^+ = 2100(\lambda_x = 2.5\delta)$. This peak location is expected given the parameters of the actuator. There is an additional peak extending through the log-region of the TBL, at the same wavelength.

Profiles of the streamwise component of mean velocity and turbulence intensity in inner variable scaling, extracted from PIV data obtained at $x = 8\delta$ are shown in Fig. 4.

In Fig. 4(a) the canonical mean velocity profile measured using PIV matches the DNS results for a canonical turbulent boundary layer with similar Reynolds number (Jiminez, 2010). There is a slight deficit in the mean velocity profile around the actuator location which extends towards the wall when the actuator plate and plasma forcing are added. This effect is mostly due to the presence of the actuator plate which creates a wake within the boundary layer. The addition of plasma forcing does not make a significant impact on the mean velocity profile measured at this downstream measurement location (Lozier et al., 2020). In Fig. 4(b) the streamwise turbulence intensity profiles measured using PIV have been corrected for spatial filtering effects, which are predicted for under resolved PIV measurements where spatial resolution leads to a loss of measured small-scale energy (Lee et al., 2016). The corrected canonical streamwise turbulence intensity profile agrees well with the DNS results. When the actuator plate is added there is a deficit in turbulence intensity created around the actuator location and within the log-region. Qualitatively, this deficit is consistent with the changes in turbulence statistics for a large eddy breakup (LEBU) device (Chan et al., 2022) positioned at a similar wall-normal location in a TBL with similar Reynolds number, shown as green triangles in Fig. 4 (b). Without active plasma forcing, the ALSSA device is similar in size and location to a common flat plate LEBU device configuration (Alfredsson and Örlü, 2018). Specifically, in (Chan et al., 2022; Chan et al., 2021) a LEBU with a streamwise length of $L = 0.9\delta$ was simulated at a wall-normal position of $H^+ = 221$ in a TBL of $Re_\tau = 480$, which is very similar to our experimental case of the TBL modified by the actuator plate alone. The slight difference in turbulence intensity deficit between the LEBU data and experimental plate only data is due to a difference in measurement location downstream of the plate. There is a slight recovery of turbulence intensity in the regions above and below the actuator location when active plasma forcing is added (Lozier et al., 2020). The center of the plasma jet was measured to be at $y^+ = 265$ (Lozier et al., 2021; Liu et al, 2022), which is above the wall-normal location of the actuator plate, $y^+ = 200$. The effect of the plasma forcing in a time averaged sense appears small as evidence in the profiles of turbulence statistics. But the plasma forcing inherently creates temporally dependent fluctuations, and as such, the phase-locked measurements presented later provide a better measure of the true effect of the plasma forcing.

In addition to the streamwise velocity components, wall-normal components of velocity have been directly measured using PIV and will be discussed here. The wall-normal turbulence intensity, Reynolds stress, and turbulence production are presented in Fig. 5. In Fig. 5(a) the measured wall-normal turbulence intensities have been compensated for spatial filtering again (Lee et al., 2016). The corrected canonical profile agrees well with the DNS results in shape but is slightly lower in amplitude across the log-region, even after correction. This difference in amplitude is likely from an underprediction of wall-normal velocity magnitudes that stem from a decrease in wall-normal sensitivity of the PIV measurements in a streamwise dominant flow, like the TBL. When the actuator plate is added there is a significant decrease in wall-normal turbulence intensity around the actuator location which extends towards the wall and above the actuator location. This reduction in wall-normal turbulence intensity around the plate location was also measured for LEBU devices (Chan et al., 2022) under similar experimental conditions, shown as green triangles in Fig. 5(a). When plasma forcing is added there is a recovery of turbulence intensity that occurs within the log-region and above the actuator. These results are consistent with the changes observed in the streamwise component of

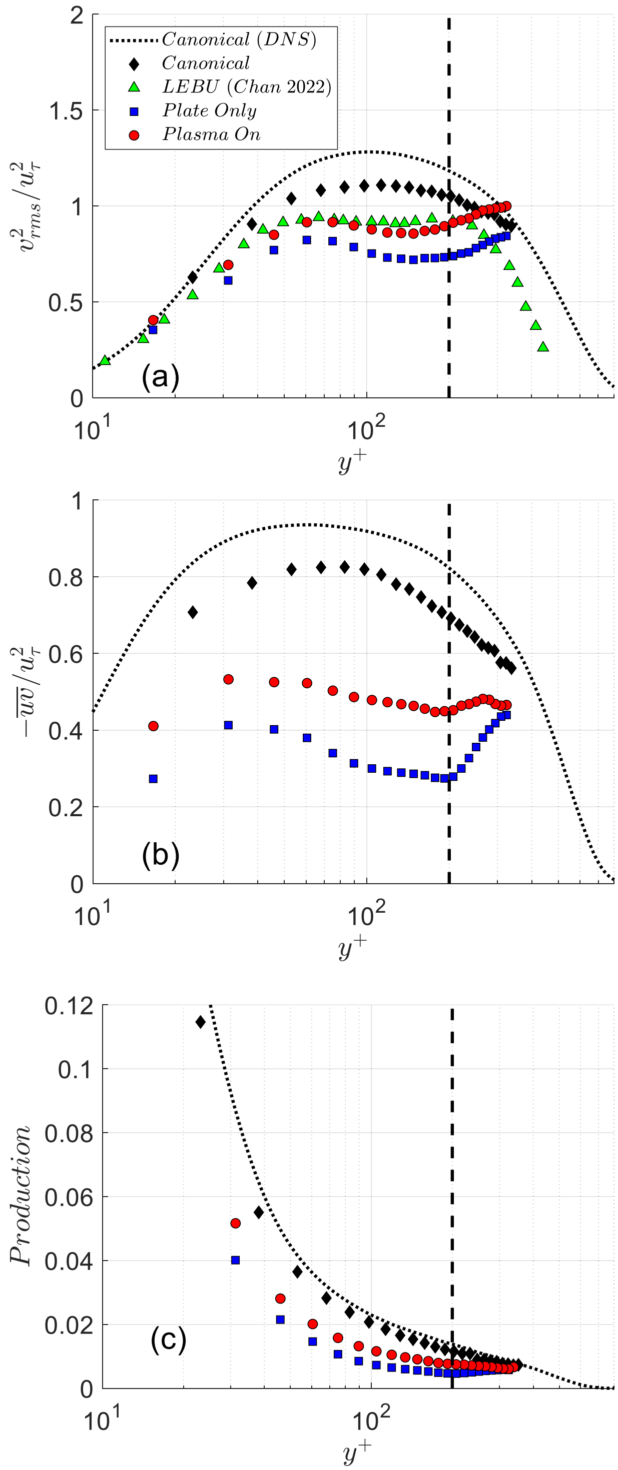

Fig. 5. (a) wall-normal turbulence intensity (b) Reynolds stress ($-\overline{uv}$)and (c) mean turbulence production $\left(-\overline{uv}\frac{\partial \overline{U}}{\partial y}\right)$. PIV turbulence intensities corrected for spatial averaging (Lee et al., 2016). Vertical dashed line indicates actuator location. Dotted line is canonical DNS data (Jiminez, 2010). Green triangles represent LES data for LEBU (Chan et al., 2022) $x = 8\delta, H^+ = 200, f_p = 80Hz$. (For interpretation of the references to colour in this figure legend, the reader is referred to the web version of this article.)

turbulence intensity as well. It is expected that for both the streamwise and wall-normal velocity components there will be a reduction in turbulence intensity around the actuator location due to the presence of the thin actuator plate and an increase or recovery of turbulent fluctuations in the region of the plasma forcing ($y^+ = 265$) which occurs directly above the actuator as described above.

In Fig. 5(b) the measured canonical Reynolds stress ($-\overline{uv}^+$) is consistently lower than the DNS data due to a combination of the spatial attenuation effects for both components of velocity as described earlier, which cannot be empirically compensated in this case. When the actuator plate is introduced, there is a decrease in the Reynolds stress around the actuator location that extends through the log-region. A reduction in Reynolds stress around the plate location was also measured for LEBU devices (Chan et al., 2022) under similar experimental conditions, though the results are not compared here because the PIV measurements are uncorrected. When the plasma forcing is activated, there is a slight recovery of the Reynolds stress at and below the actuator height.

In Fig. 5(c) the measured canonical mean turbulence production $\left(-\overline{uv}\frac{\partial \overline{U}}{\partial y}\right)$ matches the DNS results well. When the actuator is added there is a decrease in turbulence production at and below the actuator location that extends into the near-wall region. When the plasma forcing is added there is a slight increase in the mean turbulence production for this measurement location.

It is noteworthy that the profiles of mean velocity, turbulence intensity, and Reynolds stress presented here show different behaviour than the results seen in other forced turbulent boundary layers, specifically from bottom-up actuation schemes (Huynh and McKeon, 2019). In those studies, it was shown that for a wall actuated TBL case there are generally increases in the turbulence intensity and Reynolds stress in the log and outer regions of the TBL. In the present experiment, the presence of the actuator plate resulted in a decrease in these statistical quantities while the plasma jet created a slight increase or recovery of these quantities immediately above the actuator, in the region of plasma forcing, and in the log-region. The result here was an overall decrease in turbulence intensity and Reynolds stress for the current actuation scheme in contrast to the bottom-up schemes.

Since the PIV measurements were phase-locked to the plasma forcing, a phase-locked analysis (Ranade et al., 2019) of the PIV measurements was performed, where a triple phase-locked Reynolds decomposition of the streamwise velocity is used,

$$u(x,y,t) = U(x,y) + \widetilde{u}(x,y,\varphi) + u'(x,y,\varphi,n) \quad (1)$$

Here u is the instantaneous streamwise-component of velocity, U is the time mean component of velocity, $\widetilde{u}$ is a phase dependent or modal velocity component, u' is a fluctuating turbulent component, φ is the phase, and n is a number of single actuation period realizations. For the analysis presented here, the response of the TBL is primarily characterized by the root mean square (RMS) of the phase-dependent, fluctuating component of velocity, $u'_{rms}(x,y,\varphi)$. It is convenient to remove the phase-average from this quantity and investigate only the residual phase-dependent term, or the changes in the fluctuating RMS, $\Delta u'_{rms}(y,\phi)$ where,

$$\Delta u'_{rms}(y,\phi) = u'_{rms}(y,\phi) - \langle u'_{rms}(y,\phi)\rangle_{\phi} \quad (2)$$

and,

$$u'_{rms}(x,y,\varphi) = \left(\langle[u'(x,y,\varphi,n)]^2\rangle_n\right)^{\frac{1}{2}} \quad (3)$$

This new quantity $\Delta u'_{rms}$ will be used to quantify the response of small-scale turbulence to the synthetic LSS produced by the actuator and will be referred to in discussion as the residual turbulence. The same decomposition was also applied to the wall-normal, v-component, of velocity in later analysis. The same approach has been used to analyze hot-wire data in the previous studies (Lozier et al., 2021; Lozier et al., 2020).

Phase maps of the streamwise and wall-normal components of the modal velocity are shown in Fig. 6. For reference, the wall-normal location of the actuator is indicated by the dashed line. There are

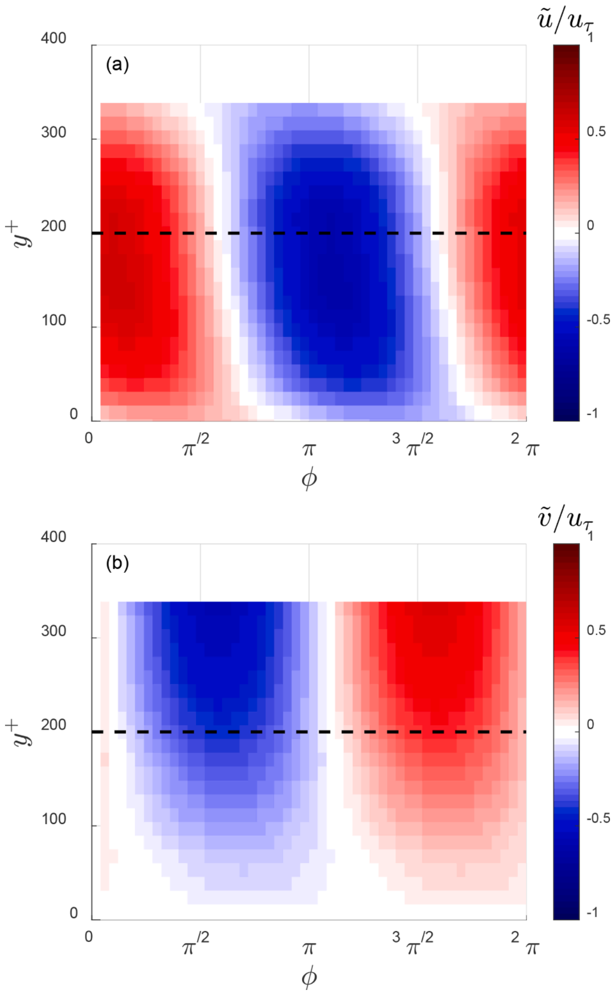

Fig. 6. Phase-dependent variations in (a) streamwise and (b) wall-normal components of modal velocity. Actuator location indicated by horizontal dashed line $x = 8\delta, H^+ = 200, f_p = 80Hz$.

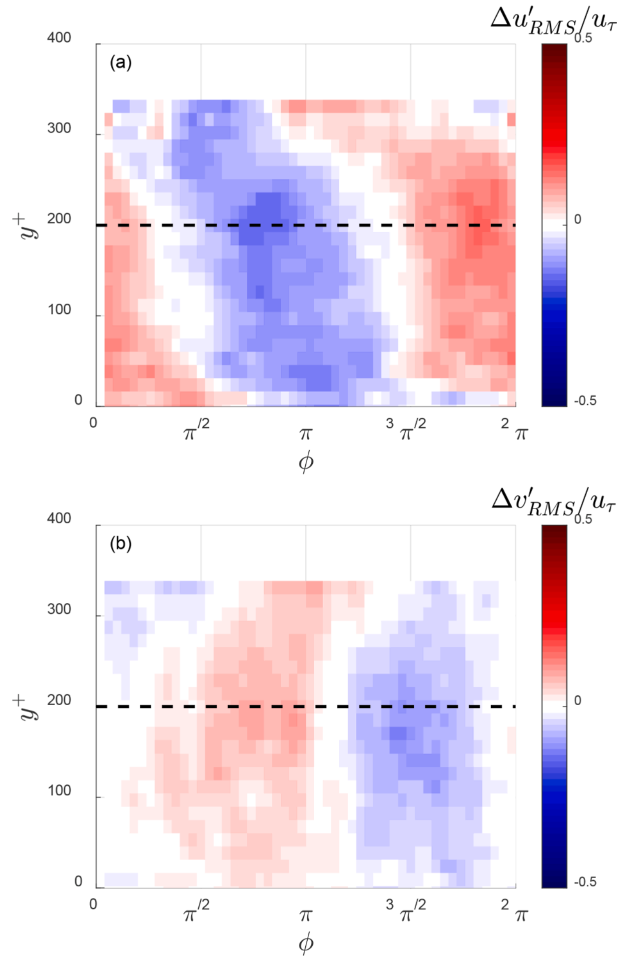

Fig. 7. Phase-dependent variations in (a) streamwise and (b) wall-normal components of residual turbulence. Actuator location indicated by horizontal dashed line $x = 8\delta, H^+ = 200, f_p = 80Hz$.

strong modal fluctuations around the actuator location that extend all the way to the near-wall region, as well as to the region above the actuator, for both the streamwise and wall-normal components. The strongest variations are between the wall-normal location of the plasma forcing, $y^+ = 265$ (Lozier et al., 2021; Liu et al., 2022), and the center of the log-region, $y^+ \approx 100$ where, theoretically, naturally occurring LSS would be present in higher Reynolds number canonical boundary layers (Guala et al., 2006). The positive fluctuations in wall-normal modal velocity appear to slightly lead the positive fluctuations in streamwise modal velocity by a phase shift of $\pi/2$. At this downstream location the fluctuations in both components of modal velocity have consistent phase across the wall-normal extent of the measurement making the fluctuations appear in a vertical column shape. These results are consistent with the hot-wire results presented in (Lozier et al., 2021; Lozier et al., 2020). In addition, the measured modal velocity agrees very well with the results of a linear spatial input–output analysis of the actuated TBL (Liu et al., 2022). The modal velocity, representative of the large-scale response of the TBL to these synthetic outer-layer LSS, is also similar to the large-scale response of the TBL to dynamic roughness observed in (Huynh and McKeon, 2019).

The streamwise and wall-normal components of the residual turbulence are presented in Fig. 7. Based on the results from previous work the phase map of residual turbulence in Fig. 7(a) can be divided into two regions for analysis. The positive fluctuations in residual turbulence above the actuator location are a signature of the convecting synthetic LSS (Lozier et al., 2021; Lozier et al., 2020). The region of positive fluctuation below the actuator will be referred to as the region of modulated turbulence. At this downstream location the two regions of the residual turbulence map have blended together and are not as spatially distinct compared to measurements immediately downstream of the actuator. The size, shape, and amplitude of the modulated turbulence, especially within the log-region, obtained using PIV is consistent with the results obtained with a hot-wire (Lozier et al., 2021; Lozier et al., 2020). The region of modulated streamwise turbulence is slightly leading in phase the positive fluctuations in streamwise modal velocity. This region is also nearly in phase with the wall-normal modal velocity near the wall. This phase relationship between the residual turbulence and wall-normal fluctuations in modal velocity suggests a possible mechanism by which transport of turbulence towards or away from the near-wall region is contributing to the modulation effect.

In Fig. 7(b) there are weaker regions of wall-normal residual turbulence, relative to the streamwise component, both below and above the actuator location. These wall-normal fluctuations in turbulence appear to have an inverse phase relationship when compared to the streamwise modal velocity.

The phase-locked decomposition process described above can also be used to study the phase-dependent changes in the Reynolds stress ($-\widetilde{uv}$). The results are shown in Fig. 8. There are strong fluctuations in the Reynolds stress around the actuator location. Above the actuator these fluctuations are in phase with the streamwise modal velocity. Near the wall the Reynolds stress appears to be $\pi/4$ ahead in phase compared to the streamwise modal velocity, while in the log-region, fluctuations in

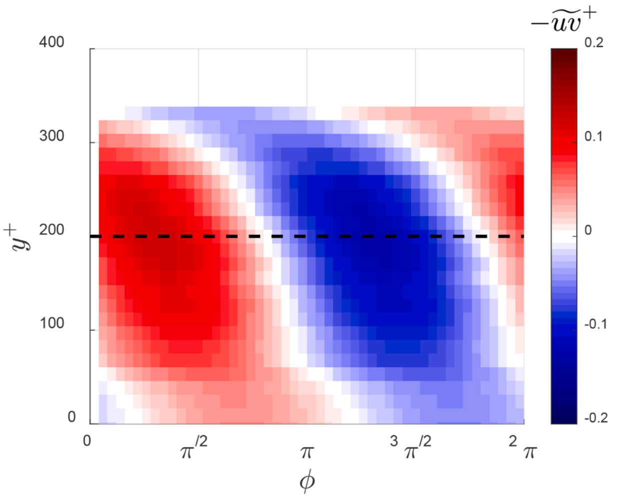

Fig. 8. Phase-locked variations in Reynolds stress $(-\widetilde{uv})$ Actuator location indicated by horizontal dashed line $x = 8\delta, H^+ = 200, f_p = 80Hz$.

Reynolds stress become in phase with the streamwise modal velocity.

These fluctuations in the modal velocity, residual turbulence, and Reynolds stress within the near-wall and log-region highlight the modulating effect of the synthetic LSS which can induce large-scale velocity fluctuations in the region between the actuator and the wall (Hutchins and Marusic, 2007; Andreolli et al., 2023). The strong changes to turbulence characteristics within the log-region, where natural coherent LSS would theoretically exist, reinforces previous observations that the actuated TBL behaves similarly to a higher Reynolds number canonical boundary layer (Lozier et al., 2021; Lozier et al., 2020) when exciting scales of motion close to the natural LSS.

Next, the phase-locked variations in spanwise vorticity and the results of quadrant splitting the modal velocity fluctuations are presented in Fig. 9. The phase dependent spanwise vorticity $\widetilde{\omega_z}$ is computed as,

$$\widetilde{\omega}_z = \frac{\partial \widetilde{v}}{\partial x} - \frac{\partial \widetilde{u}}{\partial y} \tag{4}$$

$$\Delta\widetilde{\omega}_z(y,\phi) = \widetilde{\omega}_z(y,\phi) - \langle \widetilde{\omega}_z(y,\phi) \rangle_\phi \tag{5}$$

From Fig. 9(a) the mean-removed spanwise vortical signature of the LSS above the actuator plate can be seen as well as the changes in induced vorticity in the near-wall and log-regions. The fluctuations in spanwise vorticity match the phase of the streamwise modulated residual turbulence near the wall and are π out of phase with the streamwise modal velocity above the actuator.

It should be kept in mind that a later phase corresponds to a farther upstream spatial location, if a frozen flow assumption is used,

$$x_P = x_{meas} - \frac{\varphi}{2\pi}\frac{1}{f_p}U_c \tag{6}$$

Here x_P is the streamwise pseudo-spatial coordinate, x_{meas} is the measurement location, and U_c is an appropriate convective velocity. The convective velocity in this case is based on the phase speed of the large-scale phase-locked fluctuations, and will be discussed in detail later.

From Fig. 9(b) the quadrant analysis shows that the fluctuations in the modal velocity in *physical space* follow a Q4→Q1→Q2→Q3 pattern. The quadrants were determined using the streamwise and wall-normal modal velocities to determine the pattern of large-scale motions in the actuated TBL. The observed quadrant sequence corresponds well with the dynamics of the large-scale structures observed in canonical turbulent boundary layers. This pattern has also been found to play an important role in the dynamics and transport of near-wall turbulence at smaller scales (Nagano and Tagaw, 1995). Both the vorticity and quadrant analysis results are consistent with the results of the spatial input–output analysis (Liu et al., 2022). These results demonstrate that the synthetic LSS introduced by the plasma actuator have a very similar dynamic effect on the turbulent boundary layer compared to naturally-occurring LSS in higher Reynolds number boundary layers.

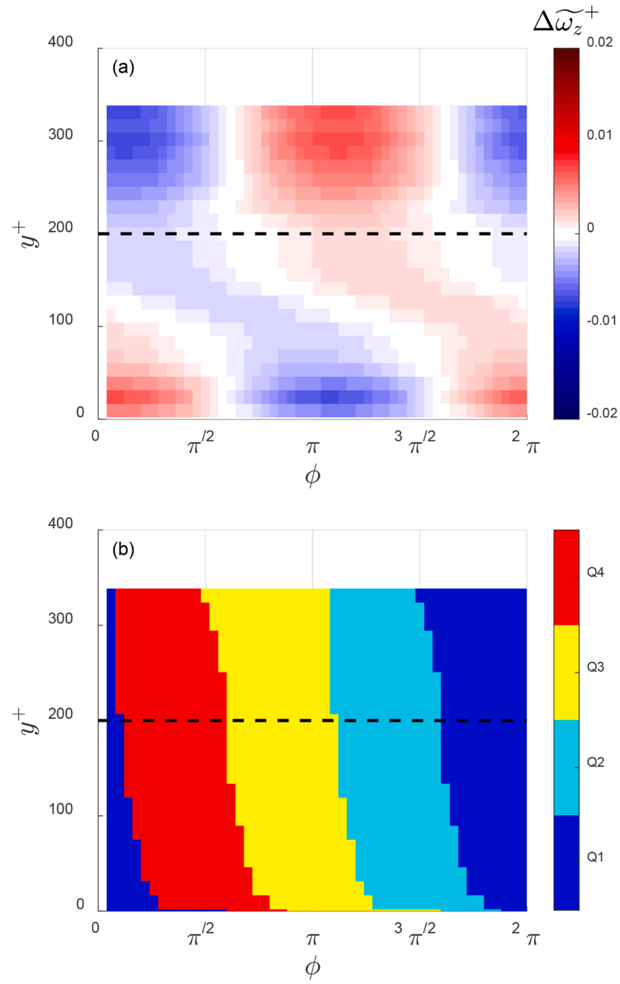

Fig. 9. Phase-locked variations in (a) spanwise vorticity and (b) fluctuating velocity quadrants. Actuator location indicated by horizontal dashed line $x = 8\delta, H^+ = 200, f_p = 80Hz$.

Using the measurements of the streamwise modal velocity presented in Fig. 6(a), the phase speed of phase-locked fluctuations at each wall-normal position were estimated by tracking the time t_n at which a maximum or minimum in the modal velocity signal arrived at each streamwise measurement station. This time t_n is related to the phase φ,

$$t_n = \left(\frac{\varphi}{2\pi} + n\right)T_p \tag{7}$$

where T_p is the forcing period. The average phase speed, u_φ, over a specific region can be found by dividing the streamwise separation between two measurement locations by the difference in computed arrival times. The same technique was applied to both the current PIV measurement and the previous hot-wire measurements (Lozier et al., 2021).

The computed phase speeds of fluctuations in the phase-locked quantities are shown in Fig. 10 as blue circles, along with the estimates of the phase speed from the hot-wire data as red squares. The mean velocity profile, presented earlier in Fig. 4(a), is shown as a solid black line in Fig. 10. Above the actuator location the phase speed follows the mean velocity profile over the wall-normal range of the current measurements. Below the actuator the phase speed is nearly constant, u_φ $19u_\tau$ $0.84U_\infty$, and is similar in magnitude to the local mean velocity measured above the actuator at the location of plasma forcing ($y^+ =$

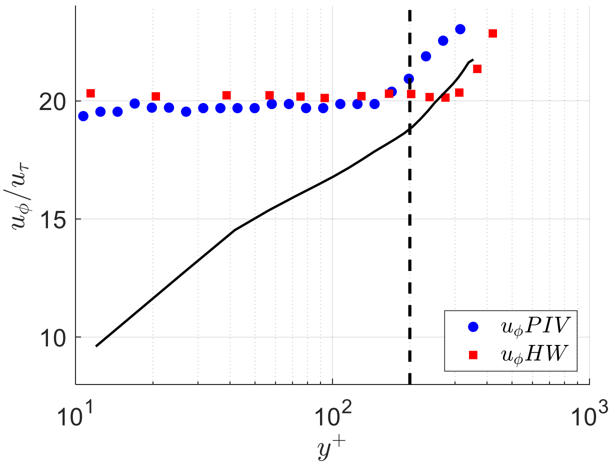

Fig. 10. Profiles of phase speed across boundary layer. Solid black line indicates mean streamwise velocity. Actuator location indicated by vertical dashed line $x = 8\delta, H^+ = 200, f_p = 80Hz$.

265). This nearly constant phase speed below the actuator suggests that any fluctuations below the actuator that are phase-locked with the plasma forcing are moving at nearly the same speed as the synthetic LSS produced by the actuator. This is additional evidence showing the modulating effect of the synthetic LSS especially within the log-region of the TBL.

Finally, using equation {6}, relating an upstream spatial location to phase, and the phase speeds computed earlier, the phase dependent measurements of quantities of interest can be reconstructed into a pseudo-spatial map to visualize the streamwise development of features in the modulated TBL. These pseudo spatial reconstructions are presented in Fig. 11 and Fig. 12.

In Fig. 11(a) the reconstructed streamwise modal velocity has a smooth transition between the reconstructed data from the measurement locations of $x = 3$ and 5δ, reinforcing the observation that the phase speed is the most appropriate analogy of convective velocity when converting phase dependence for space. There is a gap in the data downstream of $x = 5\delta$ where the reconstructed data sets do not overlap. This gap is due to the specific magnitude of the phase speeds in this experiment and the fact that only a single period of phase was used to reconstruct the pseudo spatial field for each measurement location.

In Fig. 11(b) the reconstructed map of residual turbulence is presented. The reconstructions of the modal velocity and the residual turbulence match well with previously reconstructed hot-wire data. In the map of the residual turbulence the streamwise evolution of the shape and amplitude of the region of modulated turbulence below the actuator can be clearly seen. The region of modulated turbulence starts out distinct from the signature of the LSS above the actuator but by the farthest downstream locations the positive or negative fluctuations in the residual turbulence have become a continuous region that spans most of the wall-normal extent of the measurement region as observed in the phase maps presented earlier. The peaks in residual turbulence fluctuation have been identified by black diamond markers in Fig. 11(b) to estimate the shape of the region of modulated turbulence below the actuator. At this downstream location the peaks in residual turbulence follow the dotted line marking a 20° inclination from the wall which was found to be a characteristic inclination of LSS in higher Reynolds number canonical TBLs (Hutchins and Marusic, 2007). The wall normal components of modal velocity and residual turbulence are shown in Fig. 12. The observations about the streamwise development of these wall-normal turbulence quantities are consistent with their streamwise counterparts. Farther downstream, the fluctuations become more uniform across the wall-normal extent of the measurement region.

The pseudo-spatially reconstructed results for the wall-normal and streamwise modal velocity agree well with the results of the spatial input–output analysis (Liu et al., 2022). Both the phase and amplitude are consistent around the actuator location and importantly also within the log-region and near-wall region.

4. Conclusions

The spatial–temporal response of the TBL to a periodic large-scale disturbance in the outer region was experimentally investigated using continuous laser based planar PIV. The Reynolds number of the experimental canonical TBL was low enough that there were no significant naturally occurring large-scale structures present in the outer region. Instead, the plasma actuator was used to introduce a synthetic periodic large-scale structure. The periodic nature of the synthetic LSS allowed implementation of phase-locked analysis to quantify the TBL response at multiple streamwise point locations. The PIV measurements were demonstrated to be consistent with the previous experimental work and numerical simulations, and provided new data, in the form of the wall-normal velocity, that contributed to further analysis of the actuated boundary layer. In terms of statistical quantities, the plasma-based actuation approach resulted in each turbulent Reynolds stress component decreasing in the log and outer regions. Phase-locked analysis of the modal velocity and residual turbulence showed good agreement with previous experimental work using hot-wires, as well as numerical simulations of the actuated TBL using a spatial input–output approach. Analysis of the phase-locked variations in Reynolds stress showed that the LSS have a predominantly modulating effect inside the log-region and on the near-wall turbulence. Specifically, the LSS induced velocity inside the log-region which contributes to the modulation of the near-

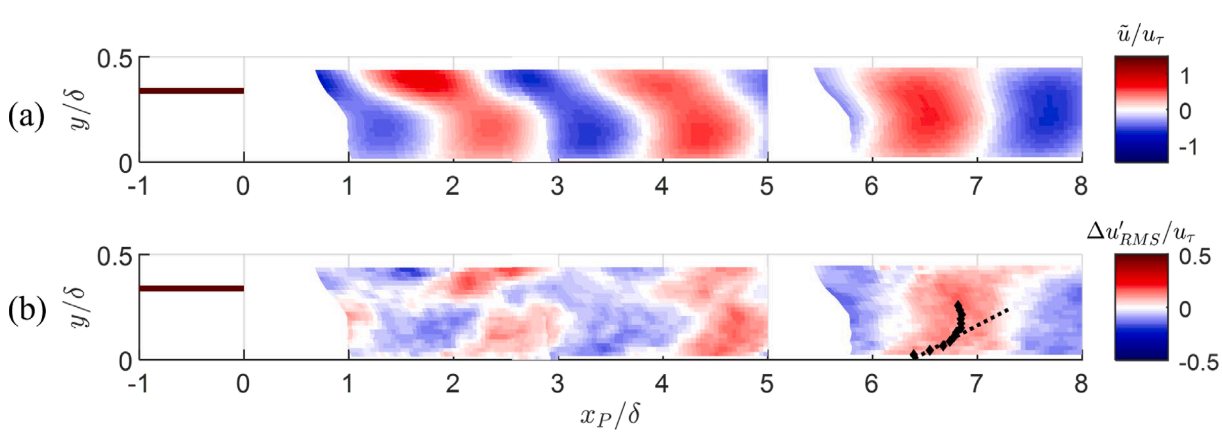

Fig. 11. Pseudo-spatial reconstruction of (a) streamwise modal velocity (b) streamwise residual turbulence. Black diamonds represent peak streamwise residual turbulence intensity. Dotted black line is 20° inclination from wall $H^+ = 200, f_p = 80Hz$.

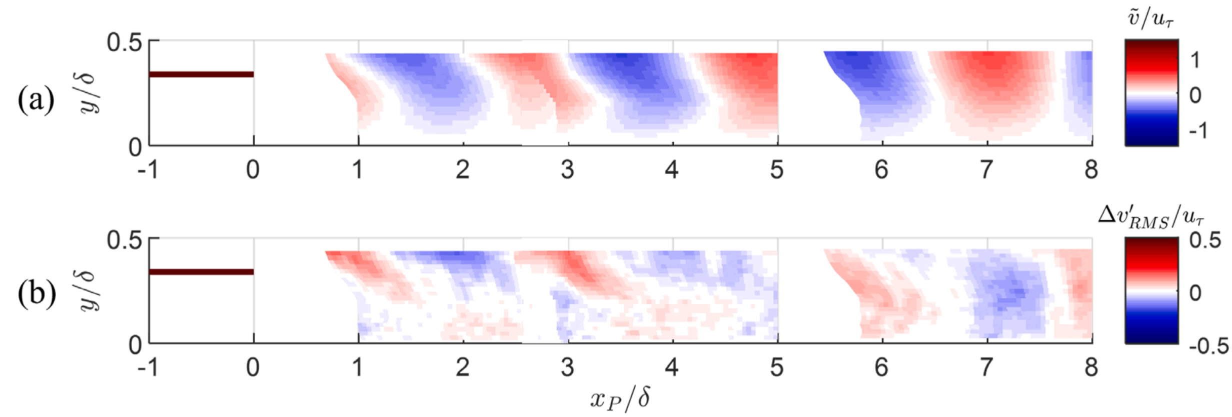

Fig. 12. Pseudo-spatial reconstruction of (a) wall-normal modal velocity and (b) wall-normal residual turbulence $H^+ = 200, f_p = 80Hz$..

wall turbulence. These observations, along with the canonical patterns shown in the quadrant splitting analysis demonstrate that the TBL is responding to the presence of LSS in a manner dynamically consistent with a higher Reynolds number canonical boundary layer. The phase speed of fluctuations in these phase-locked quantities was also computed and found to be consistent with previous experimental work. The constant phase speed below the actuator, related to the convective speed of the synthetic LSS, was observed, which provided more evidence of the modulating effect of the synthetic LSS. Reconstruction of the PIV results into a pseudo-spatial streamwise coordinate allowed for visualization of the development of turbulence characteristics. This reconstruction also highlighted the need for spatially resolved measurements over the entire downstream region to provide more information of the TBL response to the actuation.

CRediT authorship contribution statement

Mitchell Lozier: Methodology, Investigation, Formal analysis, Visualization, Writing – original draft. **Flint O. Thomas:** Conceptualization, Methodology, Writing – review & editing, Supervision, Funding acquisition. **Stanislav Gordeyev:** Conceptualization, Methodology, Writing – review & editing, Supervision, Funding acquisition.

Declaration of Competing Interest

The authors declare the following financial interests/personal relationships which may be considered as potential competing interests: Mitchell Lozier reports financial support was provided by Office of Naval Research.

Data availability

Data will be made available on request.

Acknowledgements

The authors gratefully acknowledge support from the Office of Naval Research (ONR) through grant number N00014-18-1-2534. The authors would also like to thank Dr. Igal Gluzman for his help setting up the PIV system and reducing the data.

References

Alfredsson, P.H., Örlü, R., 2018. Large-Eddy Breakup devices - a 40 years perspective from a Stockholm horizon. Flow Turbul. Combust. 100 (4), 877–888.
Andreolli, A., Gatti, D., Vinuesa, R., Orlu, R., Schlatter, P., 2023. Separating large-scale superposition and modulation in turbulent channels. J. Fluid Mech. 958, A37.
Chan, I.C., Orlu, R., Schlatter, P., Chin, R.C., 2021. The skin-friction coefficient of a turbulent boundary layer modified by a large-eddy break-up device. Phys. Fluids 33, 035153.
Chan, C.I., Örlü, R., Schlatter, P., Chin, R.C., 2022. Large-scale and small-scale contribution to the skin friction reduction in a modified turbulent boundary layer by a large-eddy break-up device. Phys. Rev. Fluids 7 (3).
de Silva, C.M., Hutchins, N., Marusic, I., 2016. Uniform momentum zones in turbulent boundary layers. J. Fluid Mech. 786, 309–331.
Guala, M., Hommema, S.E., Adrian, R.J., 2006. Large-scale and very large-scale motions in turbulent pipe flow. J. Fluid Mech. 554, 521–542.
Hutchins, N., Marusic, I., 2007. Large-scale influences in near-wall turbulence. Phil. Trans. R. Soc. A 365 (1852), 647–664.
Huynh, D., McKeon, B., 2019. Characterization of the spatio-temporal repsonse of a turbulent boundary layer to dynamic roughness. Flow Turbul. Combust. 104, 293–316.
Jacobi, I., McKeon, B., 2011. Dynamic roughness perturbation of a turbulent boundary layer. J. Fluid Mech. 688, 258–296.
Jacobi, I., McKeon, B.J., 2013. Phase relationships between large and small scales in the turbulent boundary layer. Exp. Fluids 54, 1481.
Jiminez, J., 2010. Turbulent boundary layers and channels at moderate Reynolds number. J. Fluid Mech. 657, 335–360.
Lee, J.H., Kevin, Monty, J.P., Hutchins, N., 2016. Validating under-resolved turbulence intensities for PIV experiments in canonical wall-bounded turbulence. Exp. Fluids 57 (8).
Liu, C., Gluzman, I., Lozier, M., Thomas, F.O., Gordeyev, S., Gayme, D., 2022. Spatial input–output analysis of large-scale structures in actuated turbulent boundary layers. AIAA J. 60, 6313–6327.
M. Lozier, F. Thomas and S. Gordeyev, "Streamwise Evolution of Turbulent Boundary Layer Response to Active Control Actuator," in AIAA Scitech, 2020-0097.
M. Lozier, F. O. Thomas and S. Gordeyev, "Turbulent Boundary Layer Response to Active Control Plasma Actuator," in AIAA Scitech, 2021-1455.
Mathis, R., Hutchins, N., Marusic, I., 2011. A predictive inner-outer modle for streamwise turbulence statistics in wall-bounded flows. J. Fluid Mech. 681, 537–566.
McKeon, B.J., Sharma, A., 2010. A critical layer framework for turbulent pipe flow. J. Fluid Mech. 659, 336–382.
McKeon, B.J., Jacobi, I., Duvvuri, S., 2018. Dynamic roughness for manipulation and control of turbulent boundary layers: an overview. AIAA J. 56, 2178–2193.
Nagano, Y., Tagaw, M., 1995. Coherent motions and heat transfer in a wall turbulent shear flow. J. Fluid Mech. 305, 127–157.
Ranade, P., Duvvuri, S., McKeon, B., Gordeyev, S., Christensen, K., Jumper, E.J., 2019. Turbulence amplitude amplification in an externally forced, subsonic turbulent boundary layer. AIAA J. 57, 3838–3850.
Robinson, S.K., 1991. Coherent motions in the turbulent boundary layer. Ann. Rev. Fluid Mech. 23 (1), 601–639.
Sharma, A., McKeon, B.J., 2013. On coherent structure in wall turbulence. J. Fluid Mech. 728, 196–238.